

RADIO CONTINUUM AND POLARIZATION STUDY OF SNR G57.2+0.8 ASSOCIATED WITH MAGNETAR SGR 1935+2154

R. KOTHES¹, X. SUN², B. GAENSLER^{2,3}, & W. REICH⁴

Draft version September 20, 2021

ABSTRACT

We present a radio continuum and linear polarization study of the Galactic supernova remnant G57.2+0.8, which may host the recently discovered magnetar SGR 1935+2154. The radio SNR shows the typical radio continuum spectrum of a mature supernova remnant with a spectral index of $\alpha = -0.55 \pm 0.02$ and moderate polarized intensity. Magnetic field vectors indicate a tangential magnetic field, expected for an evolved SNR, in one part of the SNR and a radial magnetic field in the other. The latter can be explained by an overlapping arc-like feature, perhaps a pulsar wind nebula, emanating from the magnetar. The presence of a pulsar wind nebula is supported by the low average braking index of 1.2, we extrapolated for the magnetar, and the detection of diffuse X-ray emission around it. We found a distance of 12.5 kpc for the SNR, which identifies G57.2+0.8 as a resident of the Outer spiral arm of the Milky Way. The SNR has a radius of about 20 pc and could be as old as 41,000 years. The SNR has already entered the radiative or pressure-driven snowplow phase of its evolution. We compared independently determined characteristics like age and distance for both, the SNR and SGR 1935+2154, and conclude that they are physically related.

Subject headings: ISM: individual (G57.2+0.8), ISM: individual (SGR 1935+2154), ISM: magnetic fields, ISM: supernova remnants, stars: magnetars

1. INTRODUCTION

Magnetars are young neutron stars with extreme surface magnetic fields, characterised by intense episodes of X-ray and γ -ray flaring (Woods & Thompson 2006; Kaspi & Beloborodov 2017). They are windows into extreme physical processes, and may also be the progenitor of time-domain phenomena such as long gamma-ray bursts and fast radio bursts (e.g., Thompson et al. 2004; Katz 2016; Metzger et al. 2017). However, the number of known magnetars is still relatively small (Olausen & Kaspi 2014), and their formation mechanisms, birth rate, evolution, and relation to other types of neutron stars are all still not understood.

Key information on magnetars can be obtained by studying their environments. Specifically, several magnetars are associated with supernova remnants (SNRs) (Gaensler et al. 2001), which provides the opportunity to make independent age and distance estimates. Each new magnetar/SNR association helps characterize the energetics and lifetime of magnetar outbursts, and maps out the progenitor and supernova phase space that can subsequently produce a magnetar.

Soft Gamma Repeater (SGR) 1935+2154 (originally named GRB 140705A) was discovered on July 14, 2005, when the *Swift* satellite detected a burst of gamma-rays and an accompanying previously unidentified X-ray source (Stamatikos et al. 2014). The source's low Galactic latitude and soft gamma-ray spectrum led Lien et al. (2014) to identify the source as a likely new magnetar, an identification that was confirmed when Israel et al. (2014) detected a 3.2-second periodicity in the X-ray emission.

Gaensler (2014) compared the position of SGR 1935+2154 to the SNR catalog of Green (2014), and pointed out that SGR 1935+2154 sits close to the geometric center of the Galactic SNR G57.2+0.8.

G57.2+0.8 was first identified by Sieber & Seiradakis (1984) in a radio continuum survey of the area surrounding the (unrelated) millisecond pulsar B1937+21, and seems to be a reasonably typical shell-type SNR. Gaensler (2014) noted that there were few SNRs in this part of the Galactic plane, suggesting a low probability of a chance coincidence between the magnetar and the SNR, and thus a good likelihood of a physical association. However, few properties of the SNR have been established, and given the history of spurious magnetar/SNR associations, the possibility of a claimed association needs to be carefully assessed.

Here we present new and archival radio data on this SNR, covering radio continuum, radio polarization and 21 cm HI observations. In Section 2, we describe the observations and data processing procedures of the Effelsberg and DRAO synthesis telescope data and present a description of the results in Section 3. An analysis of the results and their interpretation, including a thorough discussion on the possible association between SNR G57.2+0.8 and SGR 1935+2154 is discussed in Section 4. A summary and conclusions are provided in Section 5.

2. OBSERVATIONS AND DATA PROCESSING

2.1. Observations with the DRAO Synthesis Telescope

1420 MHz and 408 MHz observations were obtained with the Dominion Radio Astrophysical Observatory's Synthesis Telescope (DRAO ST, Landecker et al. 2000) as part of

¹National Research Council Canada, Herzberg Programs in Astronomy & Astrophysics, Dominion Radio Astrophysical Observatory, P.O. Box 248, Penticton, British Columbia, V2A 6J9, Canada

²Department of Astronomy, Yunnan University, and Key Laboratory of Astroparticle Physics of Yunnan Province, Kunming, 650091, China

³Dunlap Institute for Astronomy and Astrophysics, University of Toronto, 50 St. George Street, Toronto, ON M5S 3H4, Canada

⁴Max-Planck-Institut für Radioastronomie, Auf dem Hügel 69, D-53121 Bonn, Germany

the Canadian Galactic Plane Survey (CGPS, Taylor et al. 2003). Individual fields were processed using the routines described by Willis (1999) before they were mosaiced to the final data products. To assure accurate representation to the largest scales data observed with single antenna telescopes were incorporated after suitable filtering in the Fourier domain. Continuum single antenna data were derived from the 408 MHz all-sky survey of Haslam et al. (1982), from the 1.4 GHz Effelsberg survey (Reich et al. 1990), and from the second part of the Low-Resolution DRAO Survey of HI Emission from the Galactic Plane (Higgs et al. 2005) observed with the 26m John A. Galt telescope at DRAO.

For the linear polarization data, no single antenna data were added. The DRAO ST is sensitive to all structures from the resolution limit ($\sim 1'$) up to $45'$. The absence of single-antenna data is not a concern for observations of G57.2+0.8, whose maximum extent is smaller than $15'$. The DRAO Synthesis Telescope provides observations of linearly polarized emission at four frequency bands around the HI line at 1420 MHz to allow precise determination of rotation measures. Those bands are 7.5 MHz wide and the central frequencies are 1406.9 MHz for band A, 1413.8 MHz for band B, 1427.4 MHz for band C, and 1434.3 MHz for band D.

The angular resolution of the CGPS data varies slightly across the final maps as $\text{cosec}(\delta)$. At the centre of G57.2+0.8 we find a resolution of 8.5×2.8 for 408 MHz radio continuum, 2.5×0.82 for 1420 MHz radio continuum, and 2.9×0.97 for the HI data.

2.2. Observations with the Effelsberg Telescope

We conducted radio continuum observations of G57.2+0.8 at high radio frequencies including linear polarization with the Effelsberg 100-m radio telescope centered at $\alpha_{1950} = 19^{\text{h}}32^{\text{m}}50^{\text{s}}$ and $\delta_{1950} = 21^{\circ}50'$. We observed the SNR in July 1996 with the two feed 4.85 GHz receiver. In September of the same year the four feed 10.45 GHz receiver was used for three coverages of G57.2+0.8 at different parallactic angles which were combined later. At both frequencies circularly polarized components were recorded to obtain total intensity and, by IF correlation, Stokes U and Q parameters.

All observations were made in the equatorial coordinate system. The scan direction was in azimuth. The standard data reduction software package based on the NOD2 format has been applied (Haslam 1974). Individual multi-feed observations were restored by averaging the coverages obtained with the different feed. Baseline improvements by unsharp masking (Sofue & Reich 1979) were applied to the observations. The ‘‘Plait’’ algorithm described by Emerson & Graeve (1988) was used to combine coverages observed at different parallactic angles by destriping the maps in the Fourier domain. This increases the signal-to-noise ratio of the final map substantially.

The 8.35 GHz (3.6 cm) single-beam Effelsberg observations were done in May/June 2004 for total and polarized intensities. The G57.2 field was extracted from three sets of long scans running perpendicular across the Galactic plane. For details of the 8.35 GHz receiver see Kothes et al. (2006). The resulting total intensity and polarization maps are shown in Figs. 1 and 4.

G57.2+0.8 is included in the Effelsberg 11-cm (2.7 GHz) Galactic plane survey (Reich et al. 1984). It was again observed at 2.64 GHz during test observations of a new 11 cm receiver with 80 MHz bandwidth and a higher sensitivity, including linear polarization, in June 2006. The receiver concept follows those of the 4.85 GHz and the 10.45 GHz receivers. A small map centred on G57.2+0.8 was composed from 10° long scans crossing the Galactic plane. At a beamwidth of $4.4'$ G57.2+0.8 remains unresolved, thus providing total flux density, percentage polarization and polarization angle.

The resolution in the final maps is 2.6 at 4.85 GHz and 1.4 at 8.35 GHz. The 10.45 GHz observations were convolved to 1.5 to increase the signal-to-noise ratio. We found an rms sensitivity of $0.8 \text{ mJy beam}^{-1}$ in total power and $0.4 \text{ mJy beam}^{-1}$ in polarization at 10.45 GHz, about $1.3 \text{ mJy beam}^{-1}$ in total power and $0.7 \text{ mJy beam}^{-1}$ in polarization at 8.35 GHz, and $1.5 \text{ mJy beam}^{-1}$ in total power and $0.5 \text{ mJy beam}^{-1}$ in polarization at 4.85 GHz. At 8.35 GHz the given rms sensitivity is an average, since there is a rms gradient from East (low noise) to West (High noise), with a change of about a factor of 2 in sensitivity.

3. RESULTS

3.1. Radio Continuum Emission

Total power images of G57.2+0.8 are shown in Figure 1. In addition to our Effelsberg observations and the CGPS 1420 MHz data we also show the SNR at 1420 MHz taken from the VLA Galactic Plane Survey (VGPS, Stil et al. 2006) and at 74 MHz, taken from the VLA Low-Frequency Sky Survey Redux (VLSSr, Lane et al. 2012). The SNR is an almost circular source with an average diameter of about $10'$. It consists of one prominent shell to the east on-top of a smooth emission plateau with little sub-structure. The geometric centre is at $\ell = 57^{\circ}24$ and $b = 0^{\circ}81$, very close to the recently discovered magnetar SGR 1935+2154 at $\ell = 57^{\circ}25$ and $b = 0^{\circ}82$.

In Fig. 2 we display a radio map taken at 150 MHz with the GMRT as part of the TGSS (Intema et al. 2017). This is the radio map with the highest angular resolution, however, it is not sensitive to structures larger than a few arcminutes. Therefore we cannot extract an integrated flux density from this survey, but can study the detailed structures of the bright shell. The shell is divided into two parts with a clear gap in between. The southern part looks like a highly compressed shell, typical for a mature shell-type SNR. The northern part is more complex. It might consist of two separate arc-like features. The curvature of the inner one seems to be centered at the magnetar SGR 1935+2154 and the outer arc could be a continuation of the southern shell. There is a lot of underlying structure in the Northern part that may be the result of these two features interacting.

We determined flux densities from our observations and the archival 74 MHz VLSSr data (Lane et al. 2012). The flux densities were integrated in concentric rings centered at the location of the magnetar SGR 1935+2154. Newly determined flux densities are listed in Table 1. This table also contains new flux densities determined from an Effelsberg map at 2639 MHz and the 408 MHz CGPS data set, which are not displayed in Figure 1. The radio continuum spectrum of G57.2+0.8 is displayed in Figure 3. The ra-

dio spectral index α is either -0.55 ± 0.02 or -0.65 ± 0.03 , depending on whether we include the AMI high frequency measurements (Hurley-Walker et al. 2009) and the Effelsberg 10.7 GHz observation by Sieber & Seiradakis (1984). The Sieber & Seiradakis (1984) 10.7 GHz image does not cover the entire SNR, only the bright shell. Therefore this can only be considered a lower limit. Hurley-Walker et al. (2009) explain the apparent lower flux values in the AMI measurements by missing short spacings. It may also be that the full extent of the source was underestimated, because only the shell part is an obvious feature in the old observations. This would lead to an overestimate for the subtracted background emission. Therefore we take $\alpha = -0.55 \pm 0.02$ as the better estimate of the true spectral index of G57.2+0.8 over the frequency range displayed in Fig. 3.

3.2. Polarization and Rotation Measure

Images of polarized intensity with overlaid vectors in E-field direction are shown in Figure 4. Only the prominent shell is significantly linearly polarized. At 10.45 GHz the polarization signal is divided in two parts, with a “depolarization canal” (Haverkorn et al. 2004) between them. Both parts meet with an approximate 90° separation in polarization angle. A depression in total power is noticeable there, too. At 1420 MHz and 8350 MHz the total power emission structure is very similar with the same emission depression. In polarization at 1420 MHz, but also at 4850 MHz, the bottom polarization feature is very similar to 10450 MHz, but the top part is divided into two parts. The two parts are separated by another “depolarization canal” and at 4850 MHz both parts meet with an approximate 90° angle separation. At 8350 MHz the polarized intensity image is similar to 1420 MHz. Percentage polarization is at a few percent independent of frequency (see Table 1), which is low for a typical shell-type SNR. One reason might be the low angular resolution compared to the size of the SNR so that intrinsic polarization angles average out within the observing beam and reduce the fractional polarization.

We calculated a rotation measure map between 4850 MHz and 10450 GHz at the resolution of the 4850 MHz map displayed in Figure 5. We did not include the polarization observations at 8350 MHz, because of the high noise in the left part of the image, outside the shell, and the noise gradient between the Eastern and Western parts of the observation. However, we used the 8350 MHz data to determine the direction of rotation and therefore solve the ambiguity at 4850 MHz. In the PI images in Figure 4, in the bottom and centre part of the polarized emission structure, the polarization angle is rotating clockwise, leading to positive rotation measures; in the top part the polarization angle is rotating counter-clockwise resulting in a negative RM. The rotation measure calculated between 4850 MHz and 10.45 GHz is remarkably constant over the bottom PI feature and the bottom part of the top feature (see Figure 5) indicating that this “depolarization canal” is an intrinsic emission feature. There is a very steep RM gradient between the two parts of the top feature from about $+240$, like most of the SNR, to below -100 rad m^{-2} . This steep RM gradient causes the lack of polarized emission at 4850 MHz, but only causes a reduc-

tion in PI at 10450 MHz, 8350 MHz and 1420 MHz. A rotation measure of 350 rad m^{-2} would cause a rotation of only 17° at 10450 MHz, 26° at 8350 MHz, and almost 80° at 4850 MHz. At the two higher frequencies the Faraday rotation is rather low and only causes a slight depolarization. But at 4850 MHz the RM gradient seems to be just right to cause full depolarization within the beam.

It is remarkable that despite the high rotation measure of more than $+200 \text{ rad m}^{-2}$ over the bottom polarization feature, which would rotate the polarization angle at 1420 MHz by more than 500° , this feature does not seem to be “Faraday-thick” at this frequency. Here, the expression Faraday-thick refers to an effect similar to a medium being optically thick or opaque. A medium is considered to be opaque if photons cannot pass through the medium without being absorbed. A medium is considered to be Faraday thick if linearly polarized emission cannot pass through it without being depolarized.

In Figure 6 we display a sample RM determination for one pixel in this area after convolving all observations to a common resolution of $2''.6$. We made four maps around 1420 MHz for the four frequency bands provided by the DRAO Synthesis Telescope. A combined fit of all observed polarization angles results in $RM = +233 \pm 2 \text{ rad m}^{-2}$. If we use only the four bands of the DRAO ST we get $RM = +187 \pm 54 \text{ rad m}^{-2}$ and for 4850 and 10450 MHz only, we get $RM = +226 \pm 28 \text{ rad m}^{-2}$. This indicates that only smooth foreground Faraday rotation can explain the observed rotation measure and lack of depolarization with wavelength. If there were strong internal effects, the mix of synchrotron emission and Faraday rotation would highly depolarize the emission at 1420 MHz, making it Faraday thick at this frequency, and a combined fit would not be possible. Therefore the internal magnetic field in this part of the SNR must be almost perpendicular to the line of sight.

The magnetic field vectors projected to the plane of the sky are shown in Figure 5 at the resolution of the 4850 MHz measurement of $2''.6$. The vectors have been corrected for Faraday rotation. If we assume that the bright radio feature represents the expanding shell of a supernova remnant, those vectors are tangential for the bottom part and radial for the top part. This is very unusual and will be difficult to explain. In addition there is the steep RM gradient in the radial magnetic field area. The gradient seems to be mostly along the magnetic field direction displayed in Fig. 5. This can be explained by the magnetic field lines gradually bending over along the line of sight, and therefore producing significant internal Faraday rotation.

3.3. HI Data

We searched the HI data set from the CGPS and the VGPS (Stil et al. 2006) for HI shells, cavities, or filaments that might be related to G57.2+0.8 or a possible HI absorption signal. The SNR is with a peak brightness of about 12 K above the background too faint to produce a traditional absorption profile. From a comparison of HI absorption profiles of SNRs in Stokes I, Q, and U, Kothes et al. (2004) found that Stokes I profiles show excess brightness temperature fluctuation, which they attributed to emission contribution from small clouds within the beam. They suggested that for a reliable 3σ HI absorp-

tion signal the absorbed source requires a peak brightness of at least 20 K. Since the resolution of their observations are similar to ours and they also observed towards the Galactic plane, their result is immediately applicable.

There are two velocity regimes, however, where we find strong HI self-absorption (HISA) signals nearby, indicating cold and dense foreground gas. In the inner Galaxy, because of the distance ambiguity (see Figure 7), we find HISA when there is a bright background of HI emission at the far distance and a cold and dense foreground at the near distance for the same radial velocity (Gibson et al. 2005). Even though the peak brightness of G57.2+0.8 is quite low, only 12 K above the background, we find HI absorption signals towards the SNR peak in the velocity regimes that show the HISA signal (Figure 8). For the absorption profile in Fig. 7 we averaged the HI signal within the beam area of the total power peak and subtracted a background averaged over an elliptical ring surrounding the shell seen in total power. A comparison of the HISA velocity ranges with the Galactic rotation curve in the direction of G57.2+0.8 (Figure 7) gives a lower limit for the distance of about 4.5 kpc. We cannot get an upper limit from the lack of absorption at other velocities due to the low surface brightness of the SNR.

In the velocity range between about -47 and -55 km s^{-1} we found a hole, or a thick-walled structure in the HI emission that fits the SNR, in particular the bright shell, very well (Figure 9). There does not seem to be any features in velocity that may indicate the cap of an expanding HI shell. In Figure 9 at the lower negative velocities a cloud appears that turns into one thick filamentary structures that seem to wrap around the bright shell to the left and another cloud to the north-west (-44.4 $\text{km s}^{-1} \leq V_{LSR} \leq -48.0$ km s^{-1}). Towards higher negative velocities the north-west cloud disappears and the thick filament turns into a large constant surface brightness cloud, giving the impression that the SNR is sitting in a gap of HI emission. This also can explain the appearance of the SNR since there seems to be more HI material to the left and an opening to the bottom-right. To the top-left the SNR is bright indicating more material to interact with, while to the bottom-right the emission is diffuse indicating either the expansion along a density gradient or into a cavity. Towards even higher negative velocity this HI gap becomes bigger and eventually disappears.

In Figure 10 we display the radial emission profile of the SNR shell centered at the geometric centre of the SNR. It is compared with a radial profile of the HI emission calculated from an HI map that combines the velocity channels between -44.4 and -50.4 km s^{-1} displayed in Figure 9. These data have been taken from the VGPS (Stil et al. 2006), because of its better resolution. For the continuum and polarization study the CGPS data were used because of their higher sensitivity.

The relative structures of the two radial profiles seem to show that the SNR is located inside the HI hole indicated in the HI profile. This suggests that the SNR either produced this HI cavity by ionizing and sweeping up the material or this HI structure is an HI shell, maybe a stellar wind bubble produced by the supernova's progenitor star. This gives the SNR a systemic velocity in the range between -44 and -51 km s^{-1} and places the SNR in the

far Outer Galaxy.

4. DISCUSSION

4.1. Distance to SNR G57.2+0.8

Surnis et al. (2016) tried to determine a distance to G57.2+0.8 via HI absorption measurements using data from the VGPS. However, in the VGPS the SNR has a peak brightness of about 12 K above background too faint to produce a reliable absorption profile. We note that Surnis et al. (2016) did not use the brightness peak of the SNR, but chose an area of lower surface brightness about 10 K above background. As already discussed in Section 3.3 to produce a reliable HI absorption spectrum towards G57.2+0.8, the absorbed source requires a peak brightness of at least 20 K. This means that a lack of absorption in a velocity range that displays the presence of HI emission does not necessarily mean that this HI gas is behind the radio source. In addition, their chosen area for the off-profile is far too small. Larger areas have to be chosen to average out emission of smaller clouds that just happen to be at the position of the off-profile and could give the impression of an absorption signal where none exists in particular for low surface brightness radio sources. This is the case for the two absorption signals that Surnis et al. (2016) claimed to have found in their study. We inspected the HI data from the VGPS and found a cloud at the off-position for those velocities but no real absorption. Therefore their distance estimate is clearly not supported by the data.

The HI absorption signals from G57.2+0.8 we found, which correlate very well in velocity with the nearby HISA features, indicate a distance beyond 4.5 kpc for the SNR, which is beyond the tangent point in this direction of our Galaxy.

In our polarization study we also found a very high foreground rotation measure of more than $+200$ rad m^{-2} . We can compare this RM with measured values for pulsars in this area of the sky. In Figure 6 we display the rotation measure of all pulsars within 5° of G57.2+0.8 as a function of their dispersion measure (DM) distance taken from the ATNF Pulsar Catalogue (<http://www.atnf.csiro.au/research/pulsar/prscat/>, Manchester et al. 2005), version 1.56 (accessed March 31, 2017).

Recently, a new Galactic electron density distribution model was introduced to this catalogue with which dispersion measure distances to pulsars are calculated (YMW16, Yao et al. 2017). Previously, the Taylor & Cordes model was used (TC93, Taylor & Cordes 1993). Since there is a large discrepancy between the dispersion measure distances calculated with both models in the direction of G57.2+0.8, we display the results for both of them in Figure 6. The major difference between them in this direction of our Galaxy seems to be at what Galactic longitude the Sagittarius arm is contributing to the electron density along the line of sight. In the YMW16 model the Sagittarius arm is a dominant foreground feature in the direction of G57.2+0.8, while it is not present in the TC93 model above about 52° of Galactic Longitude.

In general, the foreground RM in this direction seems to be small and negative for local objects and highly positive for large distances (see Figure 6). All pulsars with RMs

above $+200 \text{ rad m}^{-2}$ are beyond 10 kpc using the TC93 model and beyond 5 kpc using the YMW16 model. Therefore, we conclude that 5 kpc is a lower limit for the SNR, which is similar to our HI absorption study. However, there is a lot of scatter in the plot, which is not surprising since the foreground is changing significantly towards the Galactic plane and Sagittarius arm.

The closest radio pulsar, PSR B1930+22, is only about $40'$ away, at Galactic coordinates $(\ell, b) = (57.35^\circ, +1.55^\circ)$. It shows $RM = 173 \pm 11 \text{ rad m}^{-2}$ and a DM distance of 9.6 kpc for the TC93 model and 8.0 kpc for the YMW16 model. There is an independent distance estimate of 10.9 kpc, based on HI absorption measurements (Verbiest et al. 2012). A comparison of the foreground RM of the pulsar and the $+233 \text{ rad m}^{-2}$ we fitted for the SNR indicates a lower limit of 10.9 kpc for the SNR's distance. Assuming that the average foreground magnetic field parallel to the line of sight is the same for both PSR B1930+22 and SNR G57.2+0.8, we can determine the SNR's foreground dispersion measure from the DM to RM ratio of the pulsar to be $DM_{\text{SNR}} \approx 290 \text{ cm}^{-3} \text{ pc}$. This results in dispersion measure distances of 9 kpc and 15 kpc for the YMW16 and TC93 models, respectively. Although all of these calculations are quite uncertain, they nevertheless indicate a very large distance well beyond the 5 kpc lower limits determined with the other methods for the SNR G57.2+0.8.

We found a systemic velocity between -44 and -51 km s^{-1} for the HI structure, which we believe is associated with the SNR G57.2+0.8. If we use a flat rotation curve for the Galaxy with the IAU endorsed values for the sun's Galacto-centric distance of $R_\odot = 8.5 \text{ kpc}$ and the Sun's orbital velocity of $v_\odot = 220 \text{ km s}^{-1}$ this velocity interval translates to a distance between 13.2 and 14.0 kpc. With the newest values of $R_\odot = 8.3 \text{ kpc}$ and $v_\odot = 246 \text{ km s}^{-1}$ determined by Brunthaler et al. (2011) the distance interval would be 12.4 to 13.0 kpc. It is already clear from those two determinations that small changes in the Galactic rotation models can cause very large differences in the distance estimate.

In the outer Galaxy in the direction of G57.2+0.8 (negative velocities), the HI emission profile in Figure 7 shows only one major emission feature. There is also only one spiral arm that far out in this direction, the Outer arm. Since the systemic velocity of G57.2+0.8 falls within the velocity range of this emission feature, the SNR must be a resident of the Outer arm. There has been a recent distance study of star forming regions inside the Outer spiral arm by Hachisuka et al. (2015). They determined distances to these star forming regions with trigonometric parallax measurements of related H_2O masers. They also fitted a logarithmic spiral pattern to their results to determine distance and pitch angle of the Outer spiral arm. We indicate the location of the major spiral arms in our Galaxy in the G57.2+0.8 velocity curve in Figure 7. Those locations are based on Figure 7 of Hachisuka et al. (2015). From their spiral pattern fit we determine a distance of $12.5 \pm 1.5 \text{ kpc}$ to G57.2+0.8 by placing the SNR in the centre of the Outer arm. The error contains the width of the arm, the uncertainty in the fit of the logarithmic spiral, and its extrapolation to the location of G57.2+0.8.

This estimate agrees within errors with the result we

derived from the flat rotation model with the R_\odot and v_\odot values determined by Brunthaler et al. (2011). However, there seems to be a shift towards higher negative velocities. This can be explained by the presence of a spiral shock in the Outer arm, which would “push” objects towards the Galactic centre. That would make them appear — from our perspective — at higher negative velocities than predicted from a flat rotation model. This has been shown for the Perseus spiral arm in the second quadrant of our Galaxy (Roberts 1972).

We will proceed by using a distance of $12.5 \pm 1.5 \text{ kpc}$ for G57.2+0.8 and assume that this SNR is a resident of the Outer spiral arm.

4.2. Structure and nature of G57.2+0.8

In our linear polarization observations, we found that part of the SNR's shell displays an intrinsic tangential magnetic field while in the other part it is radial. The observations can be explained by a typical shell-type remnant with a tangential field, part of which is overlapping with a source that contains a radial magnetic field. That would explain the depolarization canal as the place where the radial component becomes dominant and becomes stronger in general, since in total power there is an increase towards the area with the radial magnetic field. This second component could be the inner arc-like feature, which we can see in the high resolution GMRT map (Fig. 2). In our other lower resolution observations those two shells blend together, giving the impression of one thick shell.

If the pulsar produced a PWN-like feature, represented by the inner arc, with a dipolar magnetic field similar to the PWN DA 495 (Kothés et al. 2008) we could explain the large internal RM towards the magnetar and the bending over towards the shell, if we assume that we look almost into the dipole from the top or bottom. This internal dipolar magnetic field must be pointing away from us, since the foreground RM is highly positive and there is the steep gradient of less than -300 rad m^{-2} , which must have been produced internally. An internal RM of the same order of magnitude was found in the PWN DA 495 (Kothés et al. 2008). Extended X-ray emission related to the magnetar SGR 1935+2154 was found by Israel et al. (2016) and interpreted as a pulsar wind nebula. The small extent of the X-ray nebula compared to the radio nebula is typical for evolved PWNs, since the X-ray emission represents the current energy input of the pulsar and the radio emission an integration over the entire lifetime. This would make this PWN similar to DA 495 (Kothés et al. 2008).

4.3. Characteristics of the SNR G57.2+0.8

At a distance of $d = 12.5 \pm 1.5 \text{ kpc}$, the SNR's radius of about $5.5'$ translates to 20 pc. This is the average distance from the geometric centre to the outer edge of the bright radio shell. This can be seen very well in the radial profile (Figure 10). Those radial profiles determined in total power and the HI from the geometric centre match remarkably well. In HI there is a depression of about 6 K averaged over HI velocity channels of total width $\approx 7.2 \text{ km s}^{-1}$. It is not clear from the HI channel maps or the radial profile if this is a HI shell or an HI hole produced by the expanding shock wave of the supernova. Although in the radial profile it looks like an HI rim around the SNR shell, this rim

would be too wide for an expanding stellar wind bubble and the outside of that rim marks the edge of the overall HI cloud. This becomes more clear in the higher negative velocity channels displayed in Figure 9. This would make this SNR similar to CTB 109, which is also located inside a HI hole, not a stellar wind bubble, and hosts a magnetar (Kothes et al. 2002; Kothes & Foster 2012). In this case, the progenitor star should have been, similar to CTB 109, a B2 or later type star, which did not lose much material due to a stellar wind and exploded in a type II event. B1 and earlier type stars lose most of their mass in stellar winds, in particular in later stages of their evolution.

Assuming optically thin HI emission, the hole of 6 K translates to a minimum HI column density of $N_{HI} = 7.8 \times 10^{19} \text{ cm}^{-2}$ taken away by the expanding SNR. Extrapolating our radial profile, which was calculated only over the visible bright shell that makes up a segment of about 90° , to the total SNR, this indicates a mass for the swept up material of about $1000 M_\odot$ and a mean pre-supernova ambient density of about 1.2 cm^{-3} .

The simulation of radiative SNRs by Cioffi et al. (1988) gives the following equations for radius R_{PDS} and age t_{PDS} at the time a SNR enters the so-called pressure-driven snowplow or radiative phase:

$$R_{PDS} = 14.0 \frac{E_{51}^{\frac{2}{7}}}{n_0^{\frac{2}{7}}} \text{ pc} , \quad (1)$$

$$t_{PDS} = 1.33 \times 10^4 \frac{E_{51}^{\frac{3}{14}}}{n_0^{\frac{3}{7}}} \text{ yr} ; \quad (2)$$

here we assume solar abundances for the interstellar medium into which the SNR is expanding. Transforming equation 3.32a from Cioffi et al. (1988) enables us to calculate the age of the SNR from the current radius of the shockwave R_s :

$$t = \frac{3}{4} t_{PDS} \left(\left(\frac{R_s}{R_{PDS}} \right)^{\frac{10}{3}} + 1 \right) \quad (3)$$

We have estimates of the ambient medium density and the radius of the SNR, however, the explosion energy of a supernova can potentially range from a few times 10^{49} to a few times 10^{51} erg (e.g. Pejcha & Prieto 2015; Lyman et al. 2016). However, at the high end, explosion energies of several times 10^{51} erg seem to be related to more massive stars which lost most of their material in stellar winds and explode in type Ib/Ic events. But we did not find any evidence of a stellar wind bubble around G57.2+0.8 and assumed a type II event for this SNR. The radio luminosity of G57.2+0.8 between 10 MHz and 100 GHz is about $L_{radio} = 5 \times 10^{33} \text{ ergs}^{-1}$, assuming a constant spectral index of $\alpha = -0.55$ over this entire frequency range. The minimum energy required to produce this synchrotron emission is about $E_{min} = 5 \times 10^{49}$ erg, which gives us a lower limit for the explosion energy of the supernova. However, a supernova remnant with such a low explosion energy would merge with the interstellar medium before reaching such a large radius (Cioffi et al. 1988, equation 4.4b). In addition, SNRs in the radiative phase of their evolution lost already a significant amount of energy through radiation. Using equation 3.15 from

Cioffi et al. (1988), we simulated the evolution of the energy inside the SNR for varying explosion energies. We found that a minimum explosion energy of 3×10^{50} erg is necessary to retain the $E_{min} = 5 \times 10^{49}$ erg, required to produce the observed radio synchrotron emission, up to the current SNR radius of 20 pc. We assume this is a lower limit for the SNR's explosion energy. If we use the canonical value for the energy of a supernova explosion of $E_{51} = 10^{51}$ erg (3×10^{50} erg) we calculate $R_{PDS} = 13$ pc (9.2 pc) and $t_{PDS} = 12,000$ yr (9,200 yr). A comparison of R_{PDS} with the radius of G57.2+1.8 of 20 pc clearly indicates that this SNR already entered the radiative phase of its evolution. Using equation 3 results in a current age of about 41,000 yr (95,000 yr) for G57.2+1.8. We proceed to assume an explosion energy of 10^{51} erg for the supernova explosion that produced G57.2+0.8 in the following discussion.

4.4. Association between SGR 1935+2154 and G57.2+0.8

The association between the magnetar SGR 1935+2154 and the SNR G57.2+0.8 was first proposed by Gaensler (2014) based on its location at the SNR's geometric centre within uncertainties. It is argued that this is a relatively uncrowded region of the Galactic plane, which implies a high probability for a physical association. We now discuss whether independent distance and age estimates can support this association.

4.4.1. Independent Age Estimates

We found an age of about 41,000 yr for the SNR based on its spatial dimension and a constant ambient number density of $n_0 = 1.2 \text{ cm}^{-3}$. The SNR is already in its radiative phase of evolution. The characteristic age of the magnetar is $\tau = 3600$ yr (Israel et al. 2016), which is an order of magnitude shorter. The authors claim that thanks to a thorough timing analysis this characteristic age can be considered an upper limit to the real age. However, it is extraordinarily difficult to measure the age of a magnetar based on its rotation characteristics (e.g. Gao et al. 2016). The determination of the actual age of a pulsar requires knowledge about its braking index n , which in turn is determined from the pulsar's rotation characteristics including the second period derivative \ddot{P} (see equations 8 and 3 in Gao et al. 2016, respectively). This requires a constant braking index and therefore a constant \dot{P} over the lifetime of the pulsar. However, the determination of \dot{P} is very difficult because of its small value and large timing noise (Zhang & Xie 2013; Kutukcu & Ankar 2014; Haskell & Melatos 2015). In addition, \ddot{P} is strongly affected by rotational instabilities such as glitches and outbursts, which can abruptly increase P and \dot{P} (e.g. Yuan et al. 2010) and is for magnetars consequently highly variable.

Gao et al. (2016) did a study of average braking indices of magnetars constrained by the age of their host supernova remnants. Using their method (equation 10 in Gao et al. 2016) and assuming an age of 41,000 years for both, the SNR and the magnetar, we calculate a mean braking index of $n = 1.2$, similar to the value Gao et al. (2016) calculated for Swift J1834.9–0846. Gao et al.

(2016) suggest that braking indices higher than the canonical 3, typically assumed for pure dipolar fields, are caused by a decay of the magnetic field. Braking indices in the range of $1 \leq n \leq 3$ indicate an additional source of energy loss, which is attributed to a pulsar wind by Gao et al. (2016).

Although the study by Gao et al. (2016) is very speculative, it provides a possible explanation for the discrepancy between the ages determined for the SNR and the magnetar. It also adds another piece of evidence for the presence of a pulsar wind nebula, which we used to explain the unusual intrinsic magnetic field configuration derived from the linear polarization study.

4.4.2. Independent Distance Estimates

We found a distance of 12.5 kpc for the SNR G57.2+0.8. Israel et al. (2016) suggest a distance larger than 10 kpc based on the magnetar's radio inactivity, which can be linked to the X-ray conversion efficiency. Israel et al. (2016) also favour a distance much larger than 9 kpc, because of the low outburst peak luminosity at their assumed distance of 9 kpc. They fit spectra to extensive X-ray data of the magnetar observed with *Chandra* and *XMM-Newton* and found typically foreground absorption column densities of N_H between 1.6 and $2.0 \times 10^{22} \text{ cm}^{-2}$. The all-sky HI column density study by Dickey & Lockman (1990), which uses low resolution HI data and assumes optically thin HI emission, results in a total column density of $N_H = 1.2 \times 10^{22} \text{ cm}^{-2}$ to the edge of the Galaxy in the direction of G57.2+0.8. Using our CGPS HI data towards the centre of the SNR results in $N_H = 1.1 \times 10^{22} \text{ cm}^{-2}$. Dickey & Lockman (1990) suggest that HI column densities derived by assuming optically thin emission should be multiplied by 1.1 to 1.3 to account for HI self absorption. This still results in values lower than the foreground absorbing column determined with X-ray observations, but certainly indicates a large distance in the Outer Galaxy.

Surnis et al. (2016) used the empirical relation between N_H and the dispersion measure DM determined by He et al. (2013) to calculate a foreground DM for the magnetar from its absorbing HI column, resulting in a foreground dispersion measure of $420 \text{ pc cm}^{-3} \leq DM \leq 860 \text{ pc cm}^{-3}$. A comparison with the NE2001 model of free electrons in our Galaxy (Cordes & Lazio 2002) gives a distance larger than 12.5 kpc. Using the new YMW16 model (Yao et al. 2017) gives a lower limit of 11.8 kpc. However, there is a very large scatter in the N_H - DM diagram in He et al. (2013), in particular for high values of N_H . For an absorbing N_H between 1 and $2 \times 10^{22} \text{ cm}^{-2}$ DM values between 100 and more than 700 pc cm^{-3} are found. Using the average DM to N_H ratio of the 5 closest pulsars in Table 1 of He et al. (2013) gives a foreground DM for our magnetar of $270^{+70}_{-60} \text{ pc cm}^{-3}$, which is almost the same we got independently from our RM study of the SNR in section 4.1. Overall, the independent distance es-

timates of the SNR and the magnetar support a physical connection.

5. CONCLUSIONS

We have presented a thorough analysis of radio continuum and linear polarization observations of the Galactic SNR G57.2+0.8. G57.2+0.8 displays a bright radio shell in its eastern part and a smooth emission plateau that disappears into the noise towards the west. This bright radio shell consists of two narrow arc-like features when seen at high angular resolution. We found a typical overall spectral index of an evolved SNR of $\alpha = -0.55 \pm 0.02$. The linear polarization study leads to a tangential magnetic field in the lower part of the remnant and a radial field in the upper part, the latter of which could be explained by an overlapping PWN-like feature related to the magnetar SGR 1935+2154. The discovery of a small X-ray pulsar wind nebula by Israel et al. (2016) supports this assumption.

We derived an Outer spiral arm location for the SNR at a distance of 12.5 kpc. This gives the SNR a radius of 20 pc and the proposed age of about 41,000 yr make it a highly evolved radiative SNR. Based on the magnetar's location at the geometric centre of the SNR and the proximity of the independently determined distances we propose a physical association between G57.2+0.8 and SGR 1935+2154.

We like to thank Dr. Tom Landecker and Dr. Ralph Eatough for careful reading of the manuscript. We also like to express our special thanks to Harsha Blumer and Dr. Ralph Eatough for extremely valuable discussions about magnetars, their braking indices, and SNR-magnetar pairs. The Dominion Radio Astrophysical Observatory is a National Facility operated by the National Research Council Canada. The Canadian Galactic Plane Survey is a Canadian project with international partners, and is supported by the Natural Sciences and Engineering Research Council of Canada (NSERC). The Dunlap Institute is funded through an endowment established by the David Dunlap family and the University of Toronto. B.M.G. acknowledges the support of NSERC through grant RGPIN-2015-05948, and of the Canada Research Chairs program. This research is based on observations with the 100-m telescope of the Max Planck Institut für Radioastronomie at Effelsberg. The National Radio Astronomy Observatory is a facility of the National Science Foundation operated under cooperative agreement by Associated Universities, Inc. This research made use of the ATNF Pulsar Database, which can be found at <http://www.atnf.csiro.au/research/pulsar/psrcat/>. We thank the staff of the GMRT that made the observations for the TGSS possible. GMRT is run by the National Centre for Radio Astrophysics of the Tata Institute of Fundamental Research.

REFERENCES

- Becker, R. H., White, R. L., & Edwards, A. L. 1991, *ApJS*, 75, 1
 Brunthaler, A., Reid, M. J., Menten, K. M., et al. 2011, *AN*, 332, 461
 Caswell, J. L., Landecker, T. L., & Feldman, P. A. 1985, *AJ*, 90, 488
 Cioffi, D. F., McKee, C. F., & Bertschinger, E. 1988, *ApJ*, 334, 252
 Cordes, J. M. & Lazio, T. J. W. 2002, *astro-ph/0207156*
 Dickey, J. M. & Lockman, F. J. 1990, *ARA&A*, 28, 215
 Emerson, D. T. & Graeve, R. 1988, *A&A*, 190, 353
 Gaensler, B. M. 2014, *GCN*, 16533

- Gaensler, B. M., Slane, P. O., Gotthelf, E. V., & Vasisht, G. 2001, ApJ, 559, 963
- Gao, Z. F., Li, X.-D., Wang, N., et al. 2016, MNRAS, 456, 55
- Gibson, S. J., Taylor, A. R., Higgs, L. A., Brunt, C. M., & Dewdney, P. E. 2005, ApJ, 626, 195
- Green, D. A. 2014, BASI, 42, 47
- Hachisuka, K., Choi, Y. K., Reid, M. J., et al. 2015, ApJ, 800, 2
- Hamilton, P. A. & Lyne, A. G. 1987, MNRAS, 224, 1073
- Haskell, B. & Melatos, A. 2015, IJMPD, 24, 1530008
- Haslam, C. G. T. 1974, A&AS, 15, 333
- Haslam, C. G. T., Salter, C. J., Stoffel, H., & Wilson, W. E. 1982, A&AS, 47, 1
- Haverkorn, M., Katgert, P., & de Bruyn, A. G. 2004, A&A, 427, 549
- He, C., Ng, C.-Y., & Kaspi, V. M. 2013, ApJ, 768, 64
- Higgs, L. A., Landecker, T. L., Asgekar, A., et al. 2005, AJ, 129, 2750
- Hurley-Walker, N., Scaife, A. M. M., Green, D. A., et al. 2009, MNRAS, 396, 365
- Intema, H. T., Jagannathan, P., Mooley, K. P., & Frail, D. A. 2017, A&A, 598, A78
- Israel, G. L., Esposito, P., Rea, N., et al. 2016, MNRAS, 457, 3448
- Israel, G. L., Rea, N., Zelati, F. C., et al. 2014, ATel, 6370
- Kaspi, V. M. & Beloborodov, A. M. 2017, ARA&A, 55, 261
- Katz, J. I. 2016, ApJ, 826, 226
- Kothes, R. & Foster, T. 2012, ApJ, 746, L4
- Kothes, R., Landecker, T. L., Reich, W., Safi-Harb, S., & Arzoumanian, Z. 2008, ApJ, 687, 516
- Kothes, R., Landecker, T. L., & Wolleben, M. 2004, ApJ, 607, 855
- Kothes, R., Reich, W., & Uyaniker, B. 2006, ApJ, 638, 225
- Kothes, R., Uyaniker, B., & Yar, A. 2002, ApJ, 576, 169
- Kutukcu, P. & Anay, A. 2014, IJMPD, 23, 1450083
- Landecker, T. L., Dewdney, P. E., Burgess, T. A., et al. 2000, A&AS, 145, 509
- Lane, W. M., Cotton, W. D., Helmboldt, J. F., & Kassim, N. E. 2012, Radio Science, 47, RS0K04
- Lien, A. Y., Barthelmy, S. D., Baumgartner, W. H., et al. 2014, GCN, 16522
- Lyman, J. D., Bersier, D., James, P. A., et al. 2016, MNRAS, 457, 328
- Lynch, R. S., Boyles, J., Ransom, S. M., et al. 2013, ApJ, 763, 81
- Manchester, R. N., Hobbs, G. B., Teoh, A., & Hobbs, M. 2005, AJ, 129, 1993
- Metzger, B. D., Berger, E., & Margalit, B. 2017, ApJ, 841, 14
- Olausen, S. A. & Kaspi, V. M. 2014, ApJS, 212, 6
- Pejcha, O. & Prieto, J. L. 2015, ApJ, 806, 225
- Reich, W., Fürst, E., Haslam, C. G. T., Steffen, P., & Reif, K. 1984, A&AS, 58, 197
- Reich, W., Reich, P., & Fürst, E. 1990, A&AS, 83, 539
- Reich, W., Sun, X. H., Reich, P., et al. 2014, A&A, 561, A55
- Roberts, Jr., W. W. 1972, ApJ, 173, 259
- Sieber, W. & Seiradakis, J. H. 1984, A&A, 130, 257
- Sofue, Y. & Reich, W. 1979, A&AS, 38, 251
- Stamatikos, M., Malesani, D., Page, K. L., & Sakamoto, T. 2014, GCN, 16520
- Stil, J. M., Taylor, A. R., Dickey, J. M., et al. 2006, AJ, 132, 1158
- Sun, X. H., Reich, P., Reich, W., et al. 2011, A&A, 536, A83
- Surnis, M. P., Joshi, B. C., Maan, Y., et al. 2016, ApJ, 826, 184
- Taylor, A. R., Gibson, S. J., Peracaula, M., et al. 2003, AJ, 125, 3145
- Taylor, A. R., Wallace, B. J., & Goss, W. M. 1992, AJ, 103, 931
- Taylor, J. H. & Cordes, J. M. 1993, ApJ, 411, 674
- Thompson, T. A., Chang, P., & Quataert, E. 2004, ApJ, 611, 380
- Verbiest, J. P. W., Weisberg, J. M., Chael, A. A., Lee, K. J., & Lorimer, D. R. 2012, ApJ, 755, 39
- Weisberg, J. M., Cordes, J. M., Kuan, B., et al. 2004, ApJS, 150, 317
- White, R. L. & Becker, R. H. 1992, ApJS, 79, 331
- Willis, A. G. 1999, A&AS, 136, 603
- Woods, P. M. & Thompson, C. 2006, Soft gamma repeaters and anomalous X-ray pulsars: magnetar candidates, ed. W. H. G. Lewin & M. van der Klis, 547–586
- Yan, W. M., Manchester, R. N., van Straten, W., et al. 2011, MNRAS, 414, 2087
- Yao, J. M., Manchester, R. N., & Wang, N. 2017, ApJ, 835, 29
- Yuan, J. P., Manchester, R. N., Wang, N., et al. 2010, ApJ, 719, L111
- Zhang, S.-N. & Xie, Y. 2013, IJMPD, 22, 1360012

TABLE 1

INTEGRATED TOTAL FLUX DENSITIES S AND POLARIZED INTENSITIES PI OF G57.2+0.8 AT FREQUENCIES ν . THE 74 MHz FLUX DENSITY WAS INTEGRATED FROM A MAP TAKEN FROM THE VLSSR (LANE ET AL. 2012).

ν [MHz]	S [Jy]	PI [mJy]	%-pol.
74	6.50 ± 1.70	—	—
408	2.60 ± 0.40	—	—
1420	1.37 ± 0.08	52 ± 6	4 ± 1
2639	0.85 ± 0.08	15 ± 8	2 ± 1
4850	0.68 ± 0.07	22 ± 6	3 ± 1
8350	0.54 ± 0.05	11 ± 6	2 ± 1
10450	0.50 ± 0.05	30 ± 4	6 ± 1

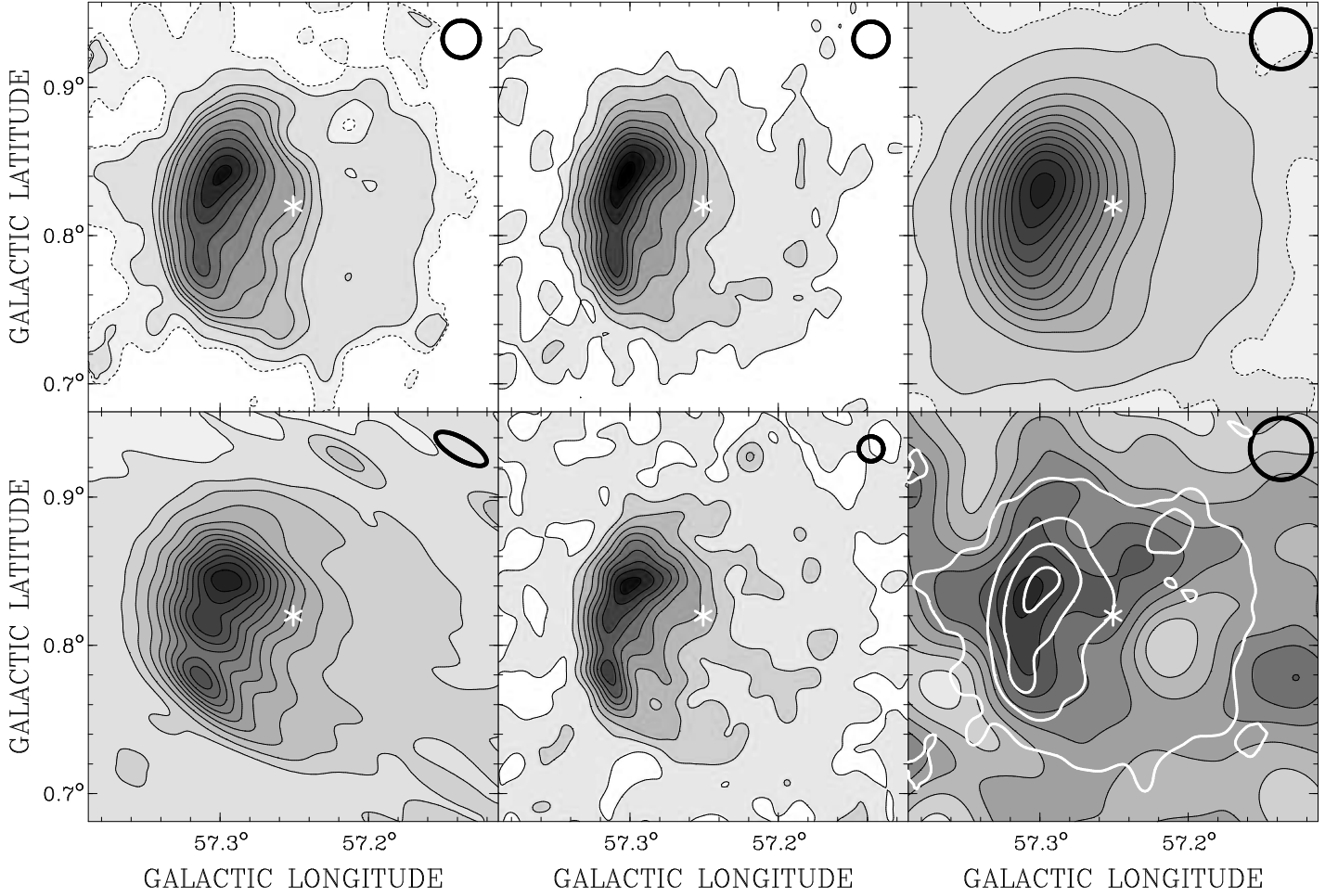


FIG. 1.— Total power maps of the SNR G57.2+0.8 at 10.45 GHz (top left), 8.35 GHz (top centre), 4.85 GHz (top right), 1420 MHz CGPS (bottom left), 1420 MHz VGPS (bottom centre), and 74 MHz (bottom right). The white asterisk indicates the location of the newly discovered magnetar SGR 1935+2154. The white contours in the 74 MHz image represent the structure in total intensity at 10.45 GHz in the top left panel. The resolution of the maps is indicated in the top right corner of each panel.

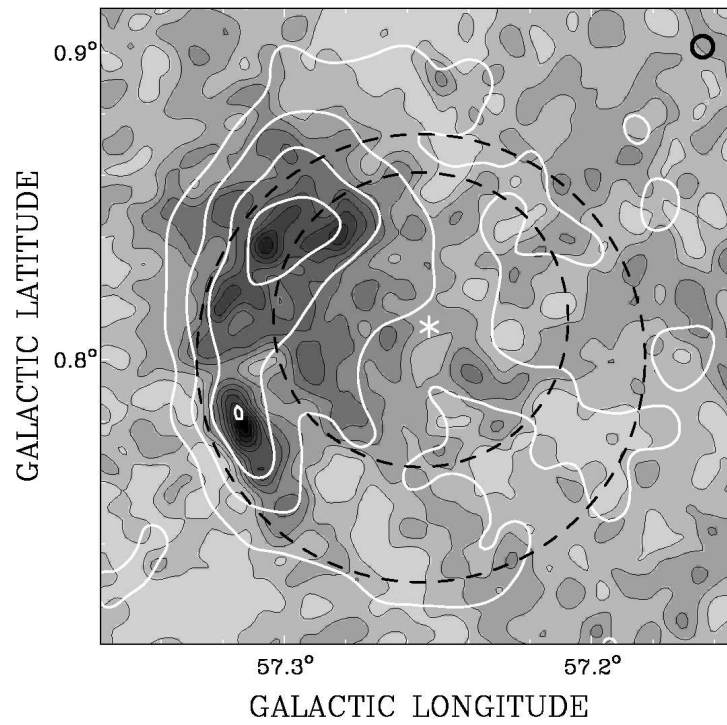


FIG. 2.— High resolution radio image taken from the first full data release of a survey of the 150 MHz radio sky, observed with the Giant Metrewave Radio Telescope (GMRT) as part of the TIFR GMRT Sky Survey (TGSS) project (Intema et al. 2017). White contours represent the VGPS observation (see Fig. 1). The white asterisk marks the location of the magnetar SGR 1935+2154. The resolution of the map is $25''$ as indicated in the top right corner of the image. The two dashed circles indicate the locations of the two arc-like features (see text).

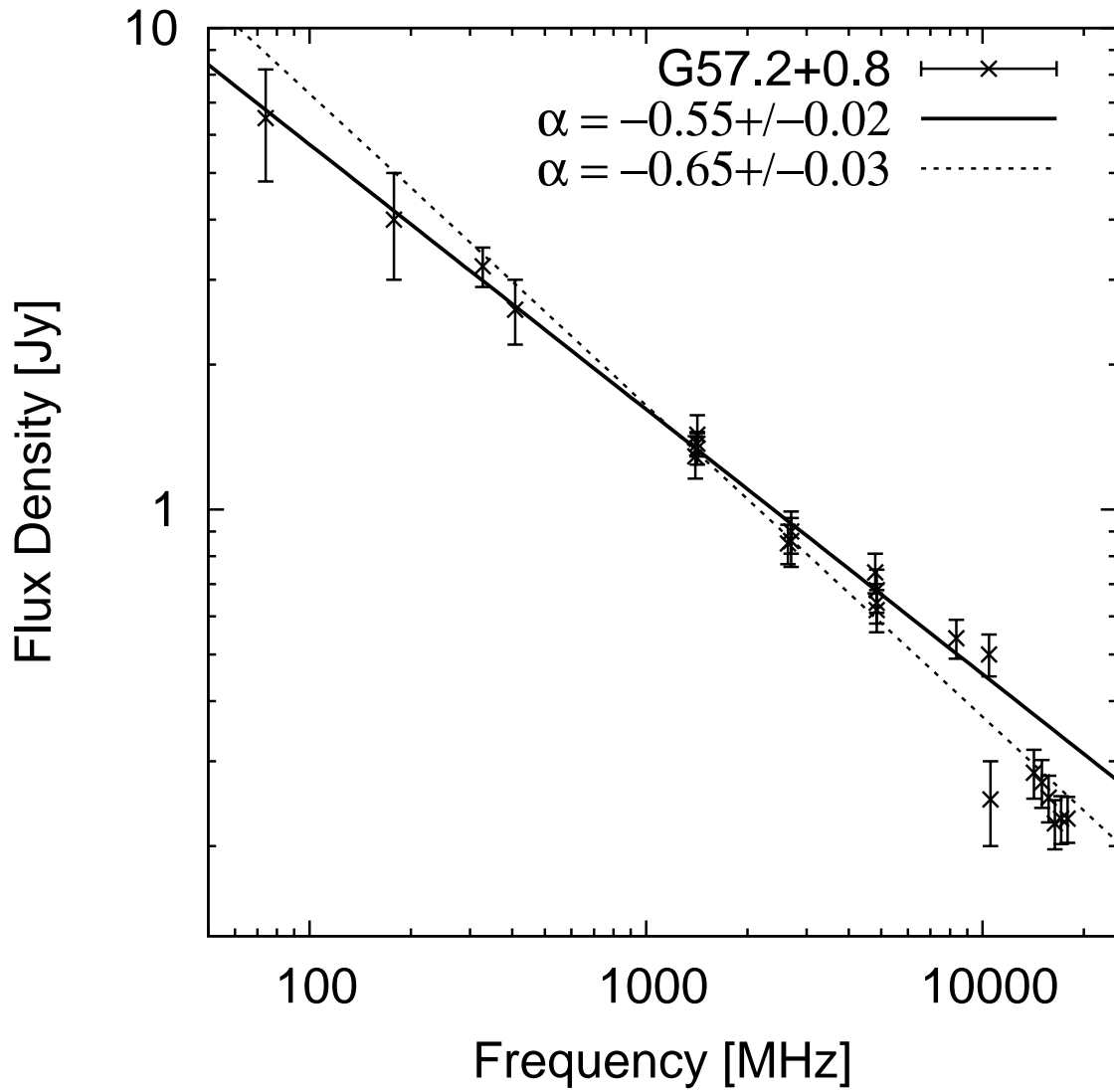


FIG. 3.— Radio continuum spectrum of G57.2+9.8. Newly determined flux densities are listed in Table 1. Archival data were taken from Reich et al. (1984); Sieber & Seiradakis (1984); Caswell et al. (1985); Reich et al. (1990); Becker et al. (1991); Taylor et al. (1992); White & Becker (1992); Hurley-Walker et al. (2009); Sun et al. (2011); Reich et al. (2014).

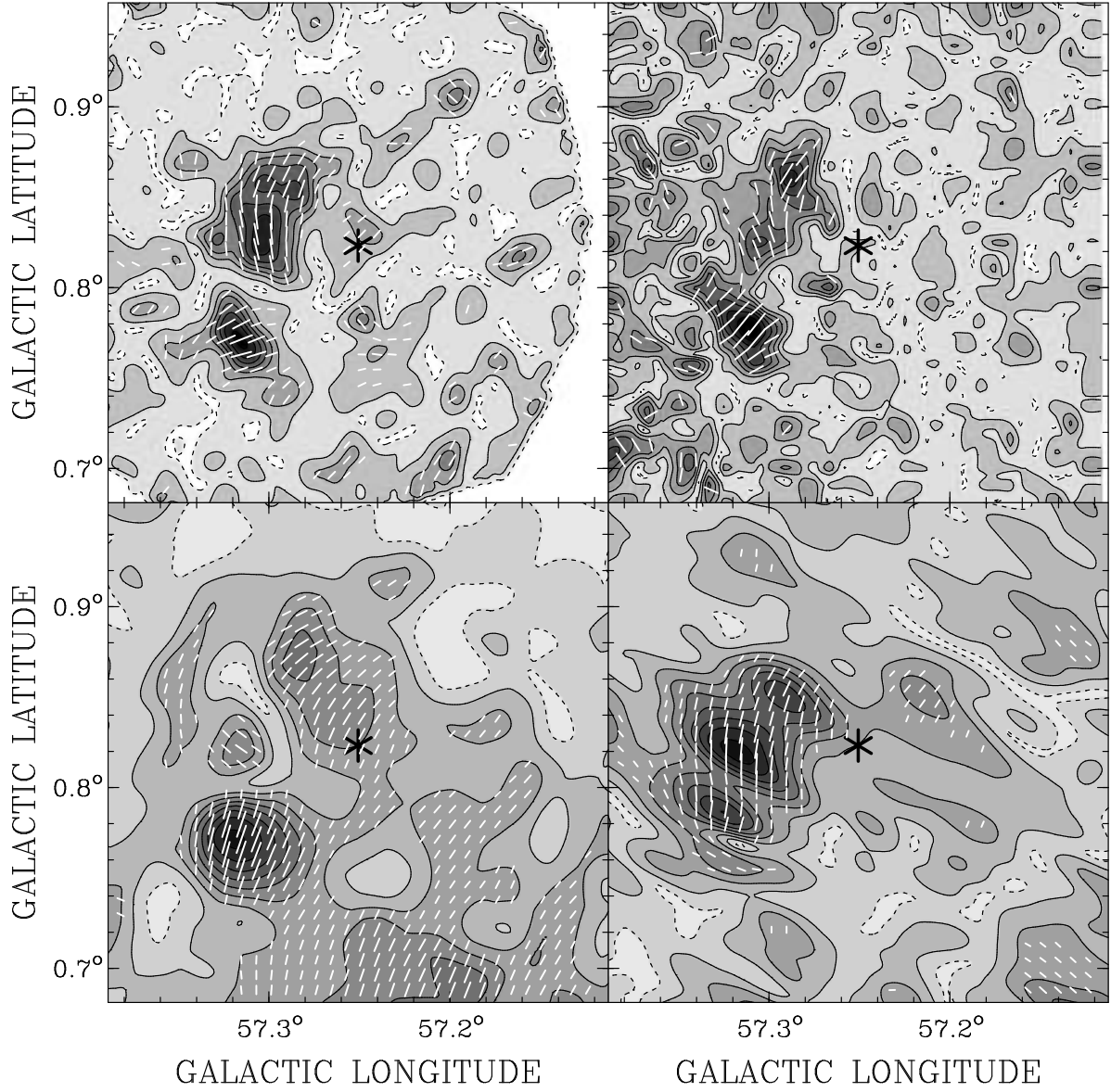


FIG. 4.— Polarized intensity maps of the SNR G57.2+0.8 at 10.45 GHz (top left), 8.35 GHz (top right), 4.85 GHz (bottom left), and 1420 MHz (bottom right). Polarization vectors in received E-field direction are overlotted in white. The black asterisk marks the location of the magnetar SGR 1935+2154.

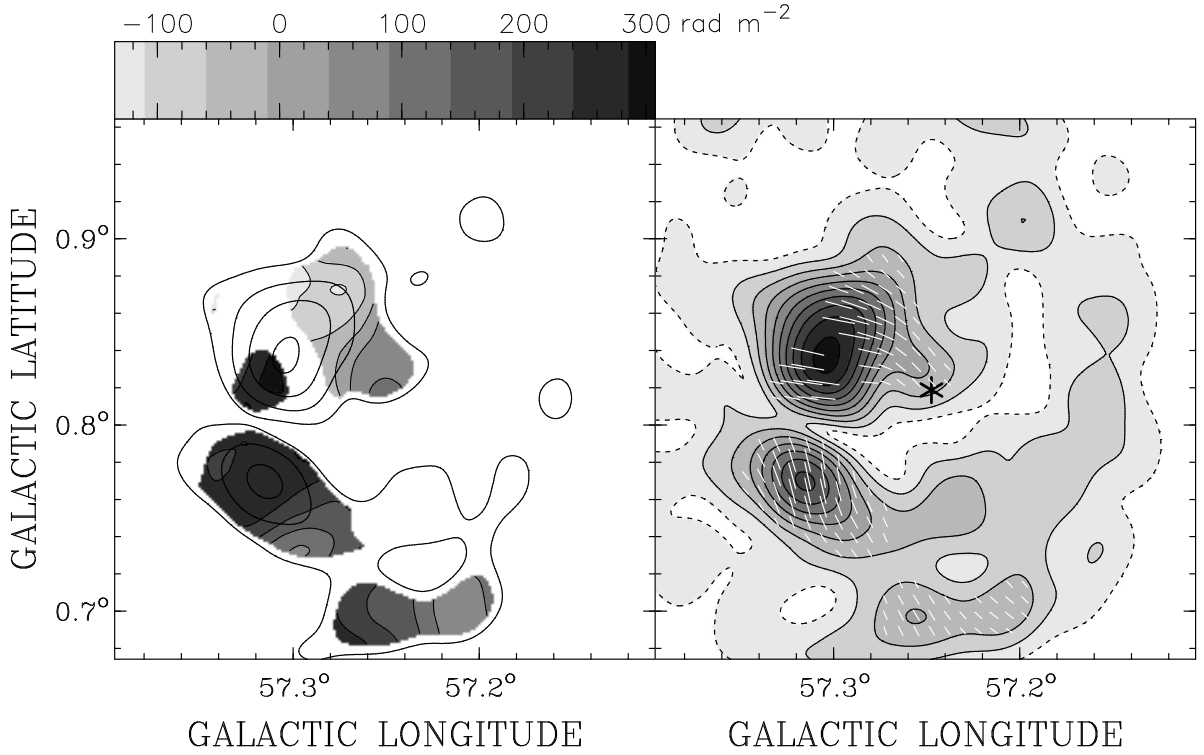


FIG. 5.— Left: Map of rotation measure calculated between 4850 MHz and 10450 MHz at a common resolution of $2''.6$. Right: Map of polarized intensity at 10450 MHz at $2''.6$. Overlaid are vectors in B-field direction corrected for Faraday rotation. The black asterisk marks the location of the magnetar SGR 1935+2154.

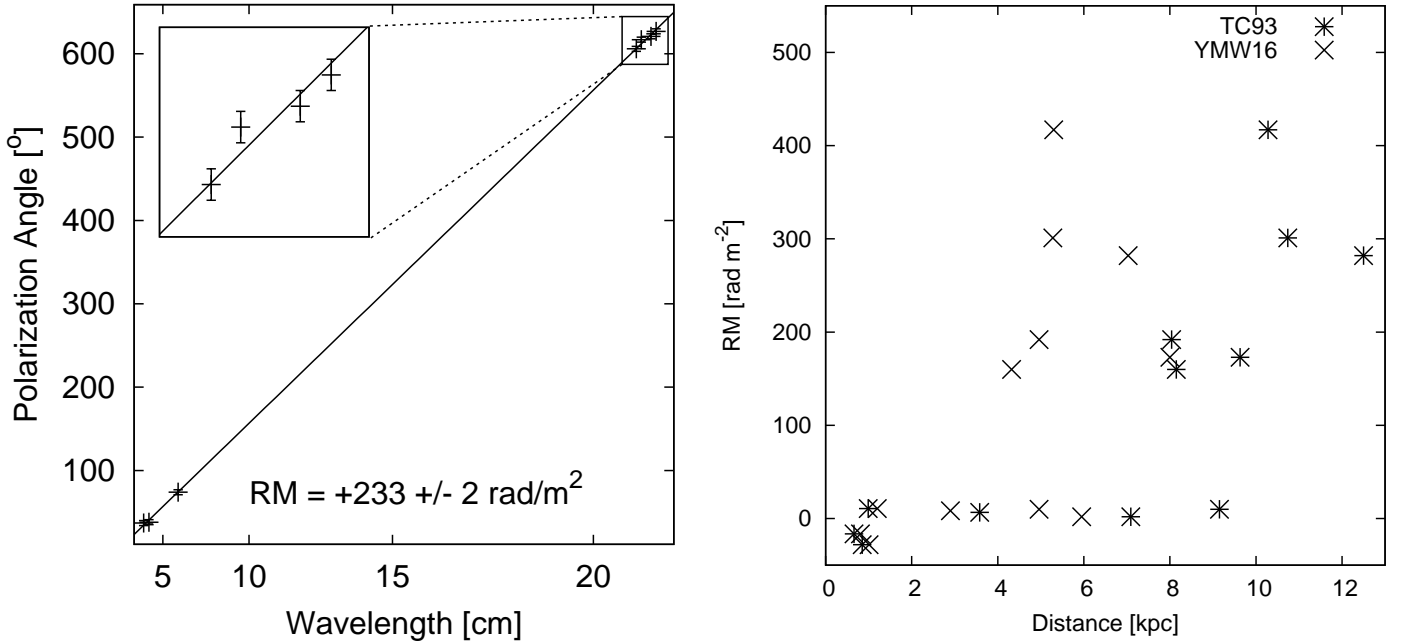


FIG. 6.— Left: Sample RM determination for one pixel in the bottom polarization feature. The inset at the top left is zoomed in on the four frequency bands around 1420 MHz provided by the DRAO synthesis telescope. Right: A plot of pulsar rotation measures as a function of dispersion measure distance taken from the ATNF Pulsar Database (<http://www.atnf.csiro.au/research/pulsar/psrcat/>, Manchester et al. 2005). All pulsars with known rotation measures within 5° of G57.2+0.8 are displayed. The rotation measures were determined by Hamilton & Lyne (1987), Weisberg et al. (2004), Lynch et al. (2013), and Yan et al. (2011). The dispersion measure distances were determined with the models by Taylor & Cordes (1993) and Yao et al. (2017).

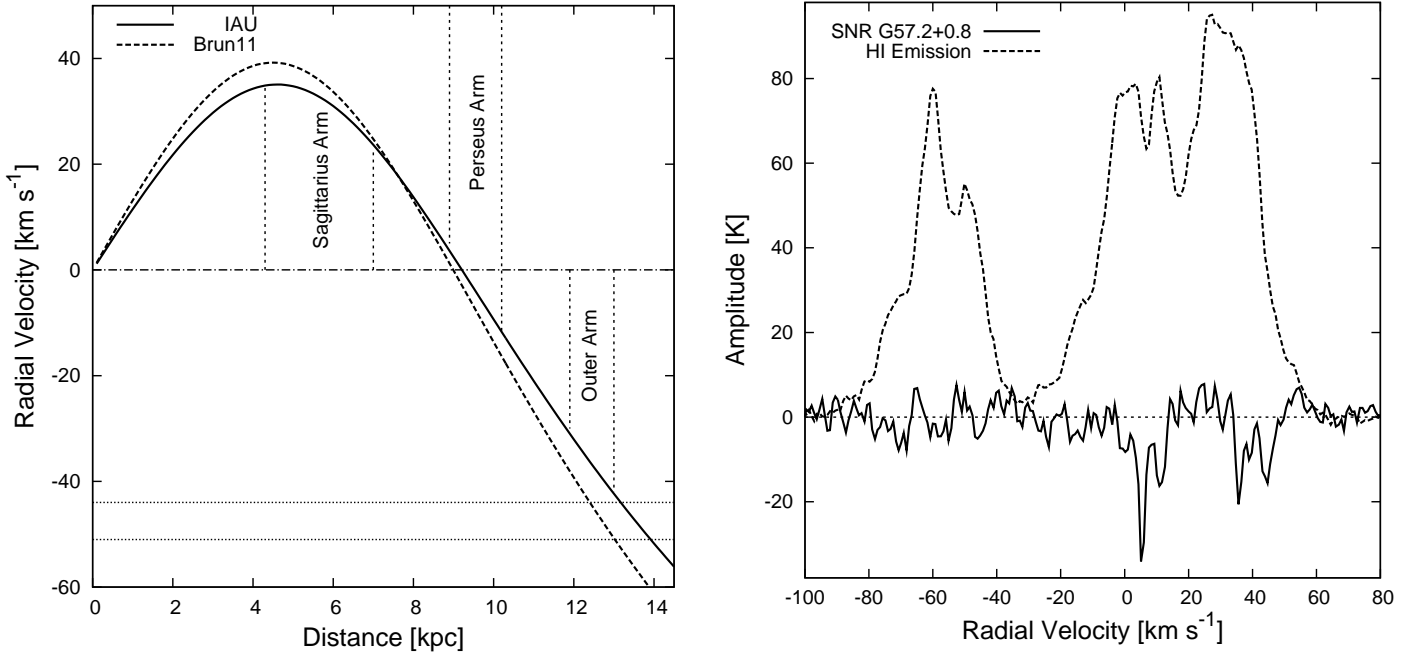


FIG. 7.— Left: Velocity field in the direction of G57.2+0.8 assuming a flat rotation curve for the Galaxy. The flat rotation model with the IAU endorsed values for the sun’s Galacto-centric distance of $R_{\odot} = 8.5$ kpc and the Sun’s orbital velocity of $v_{\odot} = 220$ km s⁻¹ is plotted as a solid line and the newly determined values of $R_{\odot} = 8.3$ kpc and $v_{\odot} = 246$ km s⁻¹ determined by Brunthaler et al. (2011) as a dashed line. Proposed locations of the spiral arms are indicated as is the proposed systemic velocity range of the SNR (see text). Right: HI absorption profile of the SNR G57.2+0.8 and the HI emission profile averaged around the SNR, which was also used as the background emission to produce the absorption profile (see text). The absorption profile has been multiplied by a factor of 2 to enhance the contrast relative to the emission profile.

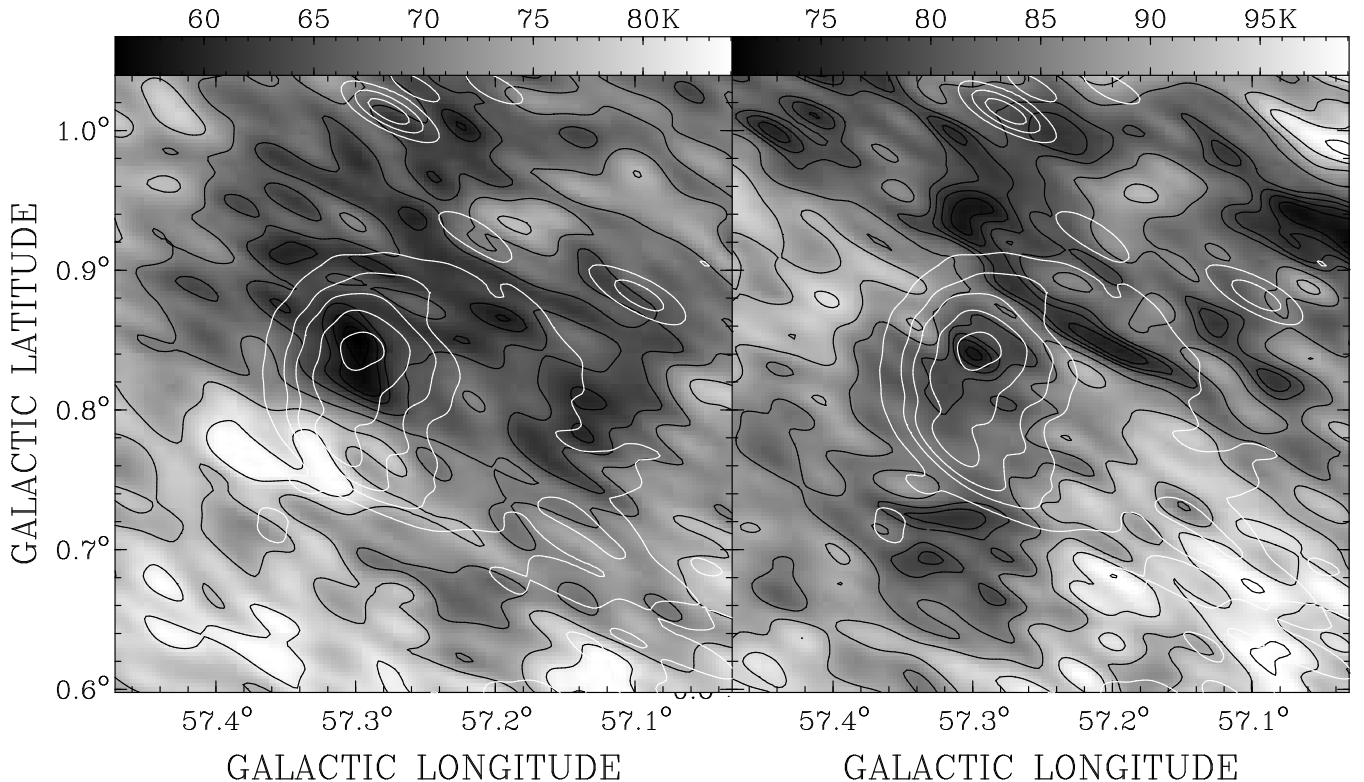


FIG. 8.— HI channel maps averaged over the absorbed velocity ranges from 5 to 7 km s⁻¹ (left) and from 35 to 36.5 km s⁻¹ (right) taken from the CGPS database. The total power emission at 1420 MHz is indicated by white contours.

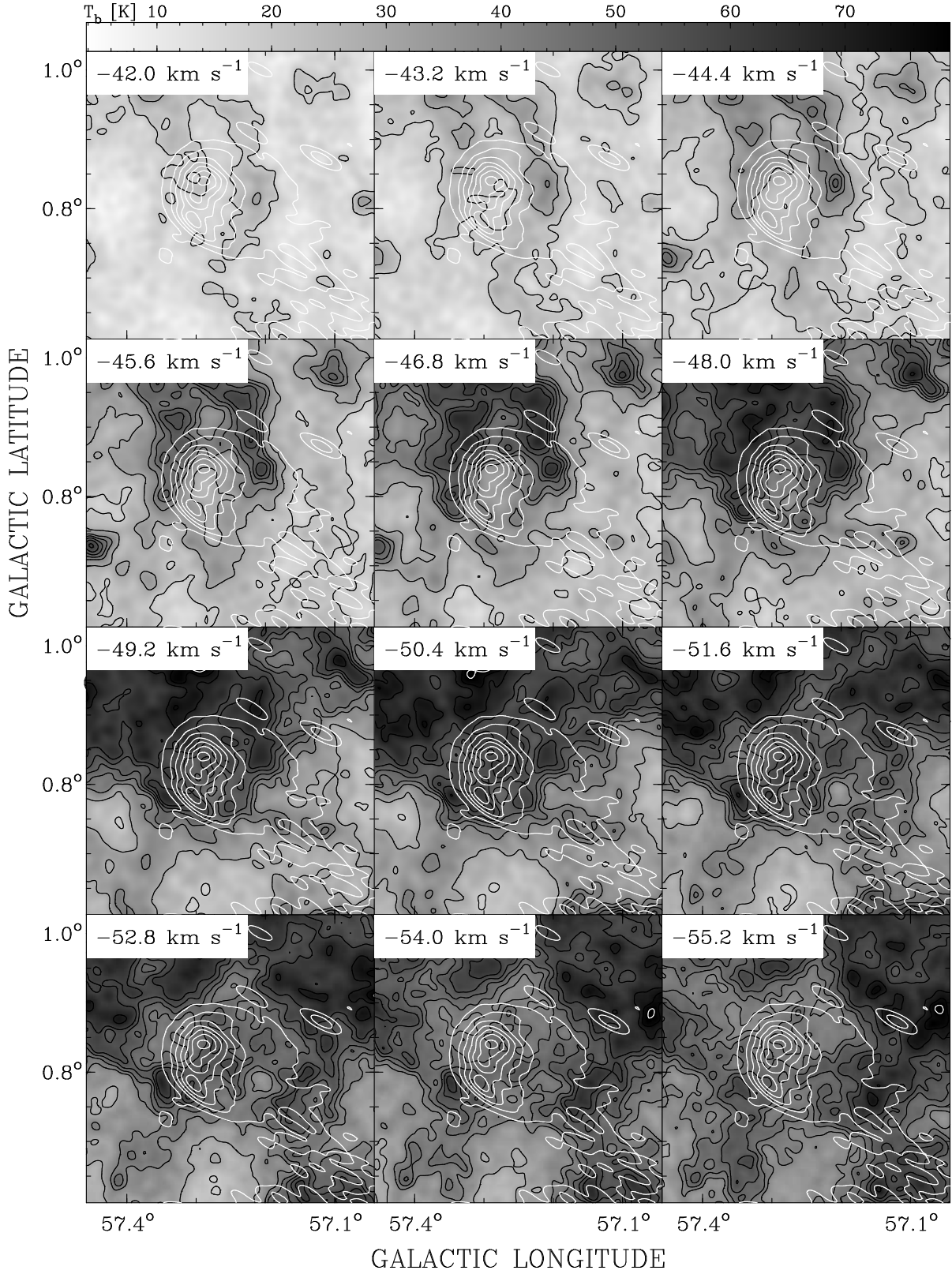


FIG. 9.— HI channelmaps in the velocity range close to the SNR's proposed systemic velocity taken from the VGPS (Stil et al. 2006). White contours indicate the total power emission at 1420 MHz taken from the CGPS (Taylor et al. 2003).

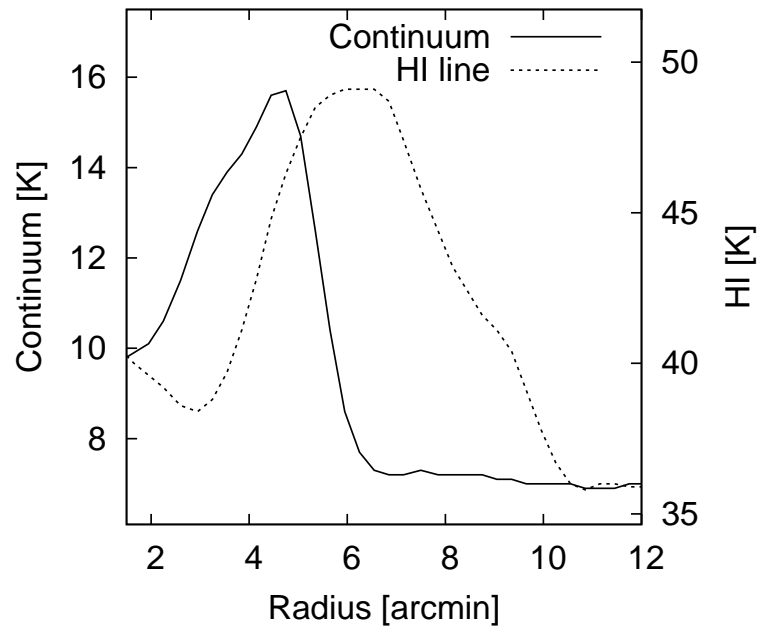


FIG. 10.— Radial profiles of the radio continuum and HI emission centered at the geometric centre of the SNR. The left Y-axis labels represent the Continuum emission and the right Y-axis labels the HI emission at 1420 MHz. The radial profile was calculated over the SNR shell only.